Published in final edited form as:

Curr Biol. 2018 March 05; 28(5): 666–675.e5. doi:10.1016/j.cub.2018.01.023.

The FERONIA Receptor Kinase Maintains Cell-Wall Integrity during Salt Stress through Ca^{2+} Signaling

Wei Feng[1], **Daniel Kita**[2,7], **Alexis Peaucelle**[3,4,7], **Heather N. Cartwright**[1,8], **Vinh Doan**[2,8], **Qiaohong Duan**[2,8], **Ming-Che Liu**[2,8], **Jacob Maman**[2,8], **Leonie Steinhorst**[5,8], **Ina Schmitz-Thom**[5,8], **Robert Yvon**[2,8], **Jörg Kudla**[5], **Hen-Ming Wu**[2], **Alice Y. Cheung**[2,*], and **José R. Dinneny**[1,6,9,*]

[1]Department of Plant Biology, Carnegie Institution for Science, 260 Panama Street, Stanford, CA 94305, USA

[2]Department of Biochemistry and Molecular Biology, University of Massachusetts, Lederle Graduate Research Tower, 710 North Pleasant Street, Amherst, MA 01003, USA

[3]Institut Jean-Pierre Bourgin, UMR1318, Institut National pour la Recherche Agronomique-AgroParisTech, Saclay Plant Science, Route de St-Cyr, Versailles 78026, France

[4]Sainsbury Laboratory, University of Cambridge, Bateman Street, Cambridge CB2 1LR, UK

[5]Institut für Biologie und Biotechnologie der Pflanzen, Westfälische Wilhelms-Universität Münster, Schlossplatz 7, Münster 48149, Germany

[6]Department of Biology, Stanford University, 371 Serra Mall, Stanford, CA 94305, USA

SUMMARY

Cells maintain integrity despite changes in their mechanical properties elicited during growth and environmental stress. How cells sense their physical state and compensate for cell-wall damage is poorly understood, particularly in plants. Here we report that FERONIA (FER), a plasma-membrane-localized receptor kinase from *Arabidopsis*, is necessary for the recovery of root growth after exposure to high salinity, a widespread soil stress. The extracellular domain of FER displays tandem regions of homology with malectin, an animal protein known to bind diglucose *in*

*Correspondence: acheung@biochem.umass.edu (A.Y.C.), dinneny@stanford.edu (J.R.D.).
[7]These authors contributed equally
[8]These authors contributed equally
[9]Lead Contact

SUPPLEMENTAL INFORMATION

Supplemental Information includes seven figures, one table, four movies, and one data file and can be found with this article online at https://doi.org/10.1016/j.cub.2018.01.023.

AUTHOR CONTRIBUTIONS

W.F., H.-M.W., A.Y.C., and J.R.D. designed the study. W.F. performed growth analysis and long-term imaging experiments and analyzed the data. A.P. and J.R.D. performed and analyzed the AFM experiments. H.-M.W. provided all molecular constructs for protein-pectin interaction and piloted binding studies. D.K. carried out the original FER-pectin interaction studies; M.-C.L., J.M., R.Y., V.D., and Q.D. produced further data based on FER and other receptor kinases to complete the receptor-pectin interaction study; and all contributed to data analysis. L.S., I.S.-T., and J.K. performed and analyzed the short-term [Ca^{2+}] imaging experiments. H.N.C. helped to establish imaging methods. W.F., A.Y.C., and J.R.D. led the manuscript-writing efforts.

DECLARATION OF INTERESTS

The authors declare no competing interests.

vitro and important for protein quality control in the endoplasmic reticulum. The presence of malectin-like domains in FER and related receptor kinases has led to widespread speculation that they interact with cell-wall polysaccharides and can potentially serve a wall-sensing function. Results reported here show that salinity causes softening of the cell wall and that FER is necessary to sense these defects. When this function is disrupted in the *fer* mutant, root cells explode dramatically during growth recovery. Similar defects are observed in the *mur1* mutant, which disrupts pectin cross-linking. Furthermore, *fer* cell-wall integrity defects can be rescued by treatment with calcium and borate, which also facilitate pectin cross-linking. Sensing of these salinity-induced wall defects might therefore be a direct consequence of physical interaction between the extracellular domain of FER and pectin. FER-dependent signaling elicits cell-specific calcium transients that maintain cell-wall integrity during salt stress. These results reveal a novel extracellular toxicity of salinity, and identify FER as a sensor of damage to the pectin-associated wall.

In Brief

For plant cells, growth requires maintenance of cell-wall integrity. Feng et al. show that salinity weakens the cell wall, which triggers FER-mediated calcium signaling to prevent root cells from bursting during growth under salt stress. The extracellular domain of FER physically interacts with pectin, indicating a potential sensing mechanism.

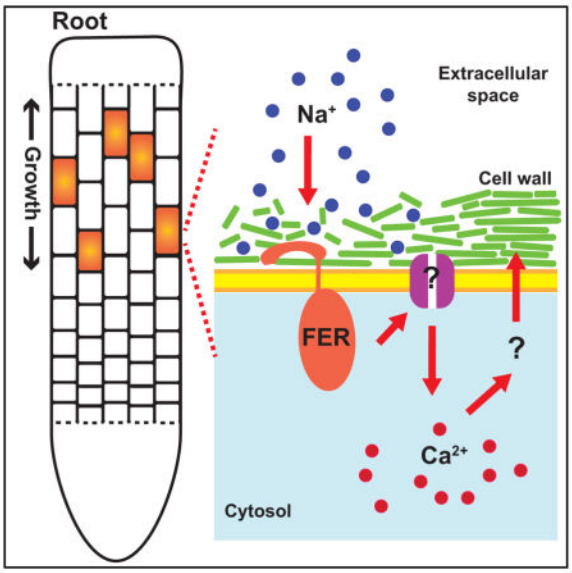

INTRODUCTION

Growth places a cell in a precarious situation. During cell expansion, structural components that limit the size of the cell must be weakened, while at the same time, homeostatic mechanisms must act to prevent a loss in cell integrity. In plant roots, these delicate processes occur in organs fully exposed to soil, where the physicochemical properties of this environment can change dramatically over the micron-length scale [1]. Excessive salinity occurs in natural and agricultural field conditions and can impose both osmotic and ionic

stress, which limit the ability of cells to take up water from the environment and cause cytoplasmic and organellar toxicity [2]. The root system responds to salt stress by dynamically regulating growth rate and direction at the organ level. Cells in the elongation zone enter a quiescent stage upon salt treatment for several hours before growth ultimately resumes [3]. The efflux carrier PIN2-mediated redistribution of auxin results in reorientation of the root tip away from the saline environment [4]. At the cellular level, salinity causes excessive radial cell expansion in roots [5], similar to genetic or chemical disruption of cell-wall integrity [6, 7]. Conversely, mutants defective in cell-wall organization are hypersensitive to salt stress [5, 8]. These data highlight a potential apoplastic toxicity of salinity stress that has not been well characterized and for which a signal transduction pathway has not been defined.

In plants, accumulating evidence suggests the existence of cell-wall integrity sensing pathways that monitor changes in wall properties [9]. Among potential cell-wall sensors, plasma-membrane-localized receptor-like kinases (RLKs), such as the FERONIA (FER)-related malectin-domain-containing THESEUS1 [10] and ANXUR1/2 [11], as well as the leucine-rich repeat (LRR) RLK, MALE DISCOVERER 1-INTERACTING RECEPTOR LIKE KINASE 2 [12], have been suggested to be involved in cell-wall sensing. Loss-of-function mutations in *FER* cause pleiotropic mutant phenotypes, including defects in female fertility, cell elongation, root-hair development, mechanosensing, and responses to hormones and pathogens [13–16]. One emerging feature of FER-dependent signaling is the downstream induction of Ca^{2+} responses [17–19]. The spectrum of *fer* phenotypes suggests that the protein may be involved in sensing a cue that is common to these biological pathways, such as a change in the properties of the cell wall.

RESULTS

FER Is Essential for Seedling Viability under Salt Stress

To investigate the potential role of *FER* in cell-wall sensing during salt stress, we challenged loss-of-function *fer* mutants (*fer-2*, *fer-4* [20, 21]) with high salinity. Compared to WT, *fer* seedlings displayed significant root growth defects within 24 hr of salt stress (Figures 1A and 1B) and were not able to fully recover their growth rate (Figure 1C). These growth defects were fully complemented by a trans-gene containing *GFP*-tagged *FER* cDNA driven by its own promoter (Figures 1A and 1B) and are consistent with the reduced root length observed for *fer* mutants under salinity in a previous study [22]. The root growth defect of *fer* seedlings is also associated with a low survival rate (12.7% ± 4.3%) compared to WT (92.2% ± 2.5%) at 2 days after salt treatment, highlighting the essential function of *FER* in salt tolerance. Salt hypersensitivity in *fer* mutants was most severe at concentrations above 100 mM NaCl, and was not observed for hyper-osmotic media containing mannitol or sorbitol with comparable osmolarity (e.g., 280 mM mannitol is iso-osmotic with 140 mM NaCl) (Figures S1A and S1B). Growth defects were observed with Na_2SO_4 (Figure S1C), suggesting that *fer* mutants are hypersensitive to the stress imposed by sodium ions, rather than the associated osmotic stress.

FER interacts with a peptide growth regulator, RAPID ALKALINIZATION FACTOR 1 (RALF1), and causes inhibition of the proton transport capacity of plasma-membrane-

localized H^+-ATPase pumps, which presumably affects growth [23]. RALF1 does not appear to have important functions in regulating growth under salt stress, as the *ralf1* mutant [23] and a *RALF1* RNAi transgenic line [24] did not show a significant growth defect (Figure 1D). These data suggest the role of FER during salt stress is largely independent of RALF1, although this does not preclude the possibility that related RALF1-like peptides are necessary signaling components in a salt-dependent pathway. Interestingly, overexpression of *RALF1*, which results in seedlings with shorter roots [24], conferred some relative resistance to salt stress (Figure 1D), which suggests that hyperactivation of the FER pathway may provide protective effects.

Consistent with our genetic analysis, treatment of *fer* mutants with the H^+-ATPase inhibitor sodium orthovanadate did not rescue growth under salt stress (Figure S1D). Instead, root growth was consistently inhibited by sodium orthovanadate treatment regardless of salt stress, suggesting that excessive proton-pump activity is unlikely to be the basis for the salinity-dependent mutant phenotype observed in *fer*.

fer Root Cells Lose Cell-Wall Integrity and Burst during Growth Recovery under Salt Stress

To determine the cellular basis for the growth defects of *fer* roots under high salinity, we performed live imaging with seedlings expressing a plasma-membrane-localized YFP marker [25]. Consistent with previous studies [5], 4D confocal imaging followed by MorphoGraphX analysis [26] revealed that WT root cells in the elongation zone began to display a loss of expansion anisotropy at the end of the quiescent stage 6–8 hr after the beginning of high-salinity treatment, and resulted in radial swelling of the outer tissue layers [5] (Figures 2A–2C; Movie S1). In the *fer* mutant, a similar loss of expansion anisotropy was initiated but quickly followed by rupturing of cells (seen as a break in the continuity of the plasma-membrane marker, and subsequently a loss of YFP fluorescence; Figures 2D–2F; Movie S1). Cell bursting occurred to such an extent that it sometimes caused a complete loss of intact cells in the outer tissues of the growth zone (Figure 2F). Tissue-specific quantification of these events in *fer* seedlings revealed that cells in the epidermal and cortical layers showed a loss of cell integrity starting 3–4 hr after the beginning of salt treatment and peaking in frequency by 7–8 hr (Figure 2H; Figures S2A and S2B). In contrast, whereas a few epidermal cells in WT also lost cell integrity after salt treatment, the frequency was much lower and was rarely observed in cortical cells (Figure 2G). We also traced the volume change of *fer* epidermal cells and found a rapid increase before cell bursting (Figure S2C), suggesting that excessive loosening of the wall may cause the loss of cell integrity. Taken together, these data reveal that FER promotes growth recovery and seedling survival during salt stress, most likely by maintaining cell-wall integrity.

The ionic, rather than osmotic, sensitivity of the *fer* mutant is similar to the *salinity overly sensitive* (*sos*) class of mutants, which are defective in excluding sodium from the cytoplasm [27, 28]. Despite this similarity, *fer* and *sos* mutants display different phenotypes under salt stress. Previous studies have shown that *sos1* and *sos2* mutant roots exhibit hypersensitivity to Na^+ and Li^+, but not K^+ [29]. This contrasts starkly with *fer*, which is hypersensitive to K^+; root growth was retarded even at 50 mM KCl or KNO_3 (Figure S2D). *fer* and *sos* mutants also displayed different sensitivities to the concentration of NaCl in the media; *sos1* and *sos2*

showed a severe reduction in growth starting at concentrations of 50 mM NaCl, whereas a considerably higher concentration (greater than 100 mM) was required to induce a similar growth defect in *fer* (Figure S3A). Furthermore, unlike *fer*, whose salt-induced loss of cell viability is restricted to the elongation zone, *sos* mutants displayed an extensive wave of cell death that spread from the elongation zone to the root tip, excluding the root cap (Figures 2I–2K; Figure S3B). These differences point to a unique growth-dependent function of *FER* in the salt response that distinguishes it from other known salt-tolerance pathways.

Previous work has shown that the glycosylphosphatidylino-sitol-anchored protein (GPI-AP) LORELEI-like GPI-AP1 (LLG1) interacts directly with FER and is required for FER localization to the plasma membrane and signaling [30]. Similar to other *llg1* mutant phenotypes, which are indistinguishable from *fer* mutant seedlings, *llg1* roots also showed the same ionic, but not osmotic, sensitivity as *fer* and similar cellular damage arising from a loss of cell-wall integrity (Figure 4C; Figure S3A). These results provide further evidence that the FER/LLG1-mediated salt-tolerance pathway is distinct from the SOS pathway.

FER Is Necessary to Reverse the Wall-Softening Effects of Salinity

To examine whether salinity and FER affect the mechanical properties of the cell wall at the root tip region, atomic force microscopy (AFM) was used. Previous studies using AFM on elongating hypocotyl tissues had plasmolyzed cells before probing, which allowed the mechanical properties of the cell cross-walls to be interrogated [31]. Here, the surface wall of epidermal cells was of greatest interest, because we observed rupturing of cells in this region; therefore, un-plasmolyzed roots were used (see STAR Methods). Within the indentation range used (less than 500 nm; Figure S4B), the force-by-indentation curves of both turgid and plasmolyzed cells similarly fit a paraboloid model (Figures S4C and S4D), suggesting that there was minimal contribution from cellular turgor within our measurements. After salt treatment, an overall drop in wall stiffness was observed in samples collected 2–4 hr after the beginning of salt treatment in both WT and *fer* (Figures 3A, 3B, 3D, and 3E), represented by a shift in the stiffness distribution curve toward lower values (Figure 3G) as well as an overall decrease in the average force measured in the elongation zone (Figure S4A). Interestingly, WT roots were able to recover wall stiffness at the beginning of the growth recovery phase, as the stiffness distribution curve is indistinguishable from non-salt-treated roots (Figures 3C and 3G). However, *fer* roots failed to restore wall stiffness before entering the growth recovery phase (Figures 3F and 3G), which may underlie the loss of cell-wall integrity.

Fortification of Pectin Cross-Links Restores Growth and Cell-Wall Integrity of fer Seedlings under Salt Stress

We hypothesized that the initial decrease in wall stiffness after salt treatment was due to the effects of sodium ions directly disrupting load-bearing ionic interactions within the wall. A particularly important component in growing cells is the pectin matrix, in which the cellulose network is embedded [32]. As a group of highly complex and dynamically modified heteropolysaccharides, pectin has been studied for its role in controlling cell-wall extensibility. The basic building block of pectin is polygalacturonic acid (PGA), which forms a hydrogel through cross-linking mediated by divalent cations. In the presence of

Ca^{2+}, gelation occurs due to the formation of intermolecular junction zones within de-esterified homogalacturonan to form the so-called egg box structure, which has been proposed to be load bearing [32]. Monovalent metal ions such as Na^+ and K^+ can displace pectin-bound Ca^{2+} and disrupt pectin cross-linking *in vitro* [33], which may underlie the hypersensitivity of *fer* to both of these ions (Figure 1B; Figures S1C and S2D).

RG-II is a sub-type of pectin unique for its use of boron to facilitate covalent dimerization that adds strength to the pectin matrix and reinforces Ca^{2+}-mediated pectin cross-linking [34]. Interestingly, whereas supplementing with borate alone only partially, but significantly, complemented the root growth defects of *fer* under salt stress, adding both Ca^{2+} and borate together nearly completely restored growth (Figure 4A; Figure S4E) and substantially reduced the cell-wall integrity defects observed in the epidermal and cortical cell files (Figures 4D–4G). These data suggest that disruption of RG-II dimerization by sodium ions may be the basis for the cell-wall integrity defects observed in *fer* mutants, as only RG-II in the wall is dependent on borate. Consistent with this hypothesis, two independent mutant alleles of *murus1 (mur1)*, which have a constitutive defect in RG-II dimerization due to loss of a sugar moiety near the dimerization site [35], exhibited a *fer*-like growth defect and cell-bursting phenotype upon salt stress, although weaker than *fer* (Figures 4B and 4C). Supplementation of borate and Ca^{2+} in the media also largely rescued the cell-bursting phenotype of *mur1* mutants (Figure 4C), indicating that the hypersensitivity to salinity of *mur1* was due to a defect in pectin cross-linking.

We also tested the contribution of other cell-wall components during salt stress. Disrupting the cellulose synthase complex by isoxaben treatment had a significant interaction with salt treatment (Figures S4F–S4H), suggesting that root growth under salinity is especially sensitive to defects in wall biosynthesis. The observed non-additive effect of isoxaben treatment is consistent with salinity impacting a non-cellulose-based component of the wall. The *xyloglucan xylosyltransferase 1,2 (xxt1,2)* double mutant, which has a reduced level of xyloglucan [36], appeared largely normal under salt stress (Figure S4I). Together, these data suggest that salinity causes a loss in cell-wall integrity during salt stress through effects on RG-II-type pectin, and these can be exacerbated through defects in other wall components.

The FER Extracellular Domain Binds Pectin In Vitro

The presence of the tandem malectin-like domains A and B (MALA, MALB) in the extracellular domain of FER (Figure S5A) and related CrRLK1L proteins suggests a potential to interact directly with cell-wall polysaccharides, such as pectin [13, 37]. To test this hypothesis, we examined the ability of a tagged FER extracellular domain (FERecd) (Figure S5B), and MALA and MALB alone, to interact with PGA, the backbone polymer of pectin. In several independent assay systems, hemagglutinin (HA)-FERecd consistently showed dose-dependent interactions with PGA (Figure 5). In affinity electrophoresis, HA-FERecd mobility was retarded in native polyacrylamide gels embedded with increasing concentrations of PGA (Figure 5A). Similarly, HA-FERecd showed a PGA-dependent mobility shift when pre-mixed with different concentrations of PGA prior to electrophoresis on a native gel (Figure 5B). The electrophoretic mobility of similarly treated BSA was not affected in these assays (Figures 5A and 5B). In dot blots and ELISA using a monoclonal

antibody that recognizes homogalacturonan (JIM5), immobilized HA-FERecd, but not several control proteins, retained JIM5-detected epitopes after incubation with increasing concentrations of PGA (Figure 5C; Figure S5C). Furthermore, when PGA was bound to membranes, maltose binding protein (MBP)-tagged FERecd, MALA, and MALB also bound to the immobilized pectin in a dose-dependent manner (Figures 5C–5E; Figures S5C and S5D). Similarly, when MBP-MALA or MBP was immobilized on amylose beads, significantly higher levels of pectin were bound to MBP-MALA-coated beads relative to control MBP-coated beads (Figure S5E). Inclusion of Ca^{2+} in the binding buffer had no discernible impact on FERecd binding (Figure S5G). The ability to interact with pectin extends to the extracellular domains of a number of FER-related receptor kinases that were tested, including BUDDHAS PAPER SEAL (BUPS1) [38], ANXUR1/2 (ANX1/2) [11], as well as the unrelated WALL ASSOCIATED KINASE1 (WAK1), as was shown previously [39] (Figures S5F and S5H). On the other hand, although all receptor kinases, with their extracellular domains located in the cell-wall milieu, have the potential to interact with its components, some react poorly with pectin, such as the LRR-domain-containing BAK1 [40] (Figure S5I).

Together, these data provide strong evidence for the MAL domains as underlying the ability for the FERecd to interact with pectin *in vitro*. Although these data do not preclude the possibility that the FERecd interacts with other components of the wall, they suggest the potential of a direct sensing role for FER to cell-wall perturbation. The observation that pectin-gelling agents mitigate the severity of *fer*'s response to salt stress (Figures 4A and 4D–4G) also supports the hypothesis that pectin-FER interactions contribute biologically to mediating salinity-induced responses.

FER Induces Cell-Specific [Ca^{2+}] Transients that Maintain Cell-Wall Integrity during Growth Recovery

FER is necessary to induce a transient increase in cytosolic [Ca^{2+}] upon mechanical stimulation, which is necessary to regulate downstream processes [17, 18]. Osmotic shock also induces a rapid calcium transient upon initial exposure to the stress; however, it is not clear whether calcium transients are also associated with late-stage responses such as growth recovery. To determine whether *FER* is necessary for salinity-induced [Ca^{2+}] transients, we utilized WT and *fer* seedlings expressing the Yellow Cameleon 3.6 (YC3.6) fluorescence resonance energy transfer (FRET) [Ca^{2+}] sensor [41] and imaged seedlings once every 15 s at the root tip region for up to 15 hr during salt treatment. These extended imaging sessions revealed never-before-described cell-specific [Ca^{2+}] transients occurring mostly in the early elongation zone (Figures 6A–6C; Movie S2), which were absent in roots transferred to standard media (Figure S6A). These transients were localized to individual cells and persisted for less than a minute (Figures 6A–6C; Movie S2). Kinematic analysis of growth at the root tip clearly showed that these [Ca^{2+}] transients were correlated spatially and temporally with growth recovery (Figures 6D and 6F; Movie S3). Importantly, these late-stage calcium transients were strongly reduced in frequency in *fer* mutants (Figure 6E; Figure S6D; Movie S3), which correlates well with their inability to recover growth (Figure 6G; Figure S6E). WT roots treated with 280 mM mannitol (same osmolarity as 140 mM

NaCl) or 100 mM NaCl showed far fewer [Ca^{2+}] transients, which is consistent with the lack of a *fer*-dependent growth defect under these conditions (Figures S6B–S6E).

To test whether these FER-dependent [Ca^{2+}] transients are necessary to maintain cell-wall integrity, we transferred WT seedlings that were pre-treated with salt for 5 hr to media containing a plasma-membrane Ca^{2+} channel inhibitor, $LaCl_3$. This treatment greatly reduced the number of cell-specific [Ca^{2+}] transients (Figure S6F) and resulted in severe cell bursting (Figures 6H and 6I; Movie S4). Similarly, EGTA, a Ca^{2+} chelator, also induces WT cell bursting after salt treatment, although less severely and with a slightly different temporal profile (Figures S6G–S6J). These data are consistent with the hypothesis that the loss of cell-wall integrity observed in *fer* mutants is a consequence of the reduction in late-stage cell-specific [Ca^{2+}] transients. [Ca^{2+}] transients induced upon immediate exposure to NaCl or mannitol treatment occurred outside of the growth zone in WT, and these were generally weaker in *fer* mutants (Figure S7); however, the lack of exclusively salinity-specific defects in these particular transients suggests that they are not directly involved in the maintenance of cell-wall integrity that occurs several hours later. Ectopic [Ca^{2+}] transients were observed in the *fer* elongation zone, and suggest localized hypersensitivity of *fer* mutants to salt stress.

DISCUSSION

Here we report that salinity has a direct impact on the mechanical properties of the cell wall, revealing a previously unknown apoplastic toxicity of sodium ions and, more broadly, monovalent metal cations. We show that the RLK FER is necessary for the acclimation of seedlings under high salinity and that lack of FER-dependent signaling leads to cell rupture, most likely due to the inability of cells to sense and compensate for the weakening of the wall. FER-dependent defects under high salinity can be counteracted by treatment with pectin-gelling agents, and mutants that disrupt pectin cross-linking show *fer*-like defects in maintaining cell-wall integrity. Together, these data support a model in which high salinity weakens the wall by disrupting pectin cross-linking. Damage to the wall is most likely exacerbated when turgor pressure is restored and tension on the pectin matrix increases, as cells in the elongation zone reactivate cell expansion during the growth recovery stage of the salt-stress response [3]. Such growth-dependent damage may be sensed by FER through its pectin-binding extracellular domain and lead to a rapid cell-autonomous increase in cytosolic [Ca^{2+}], which regulates downstream cellular events necessary to prevent a loss of integrity (Figure 7).

FER, as well as other members of the CrRLK1L family, also maintain cell integrity in tip-growing cells, such as root hairs and pollen tubes [11, 20]. Tip-growing cells expand through localized softening of the wall, a process that makes these cells susceptible to rupture. Whereas other cell types normally lack such defects in *fer*, salt stress induces similar bursting in non-tip-growing cells. That salt stress induces bursting even in non-tip-growing *fer* cells reflects enhanced susceptibility of the mutant cell wall to salt-induced weakening. Interestingly, pectin is particularly prominent at the apex of tip-growing cells, and its cross-linking dynamics are crucial for tip growth [42]. Thus, we speculate that FER-based signaling may be particularly important in regulating cell growth that heavily relies upon pectin cross-linking.

A physical interaction between the extracellular domain of FER and pectin was detected *in vitro*, suggesting that cell-wall properties may be directly monitored by FER. However, it is important to emphasize that such binding does not necessarily demonstrate direct sensing, as it still remains to be tested whether pectin fragments can directly activate FER signaling. WAKs are another group of RLKs that can bind to pectin, especially oligogalacturonides (OGs), which are released upon pathogen infection or wounding [43]. However, the role of WAKs in abiotic stress response is largely unknown. Recently, very short OGs were found to serve as a dark-associated signal to regulate hypocotyl elongation during skotomorphogenesis [44], suggesting a more general role of OGs as signaling molecules. It is possible that OGs of different lengths can be recognized by different receptors and trigger unique responses. It will be interesting to test whether such pectin fragments are also released during salt stress and can activate FER signaling.

Pectin-FER interactions themselves may be sensitive to monovalent cations *in muro*, or perhaps changes in wall integrity may affect the interaction of FER with other signaling partners such as RALF-like peptides [23]. Although the molecular details of how such interactions trigger signaling remain to be determined, our results clearly demonstrate that salt stress impacts a FER-dependent signaling pathway that leads to a rapid cell-autonomous increase in $[Ca^{2+}]$ during the growth recovery stage and prevents cell bursting under high salinity (Figure 7). These rapid cell-scale $[Ca^{2+}]$ transients reveal spatial heterogeneity in the acclimation status of cells within the organ, and highlight the important role that cell-autonomous signaling plays in enabling cells to keep pace with growth of the tissue as a whole.

Our work suggests that regulation of wall chemistry may be an important salt-tolerance mechanism. Recent characterization of the seagrass (*Zostera marina*) genome revealed an expansion in the number of genes encoding pectin methylesterases, consistent with the relatively low degree of methylation in seagrass pectin [45]. It will be interesting for future studies to determine whether pectin modification (e.g., by providing a mechanism to modulate/regulate cross-linking in the wall matrix) also plays a role in enabling salt tolerance in glycophytes such as *Arabidopsis*.

FER functions in a diverse number of pathways and mediates sensing of abiotic and biotic cues [13, 46]. We have found through transcriptome analysis of *fer* mutant roots that of the 415 WT-specific salt-induced genes there is substantial enrichment for biotic stress and defense responsive genes, such as those induced by chitin (Table S1; Data S1). Indeed, Espinoza et al. recently demonstrated that salt stress induces a chitin-like transcriptional signature that is dependent on CERK1, the chitin receptor [47]. Induction of biotic-stress-associated transcriptional responses under salt stress may be due to the coupling of FER, a DAMP (damage-associated molecular pattern) receptor, with MAMP (microbial-associated) or PAMP (pathogen-associated) receptors at the plasma membrane. The stress hormone abscisic acid (ABA), which is induced by salt stress [3], dampens biotic-stress signaling [48], and it may be that specificity in the pathway is established through other abiotic stress cues. Alternatively, lack of coherent DAMP and MAMP/PAMP cues could cause these responses to be short lived. This model of FER signaling may apply to other functions that

this receptor plays, where coherence of different signaling cues refines the downstream functions that wall sensing ultimately elicits.

STAR★METHODS

KEY RESOURCES TABLE

REAGENT or RESOURCE	SOURCE	IDENT
Antibodies		
JIM5	CCRC [20] and Dr. Paul Knox [49]	JIM5
M38	CCRC [20] and Dr. Paul Knox [49]	M38
mouse anti-HA antibody	Santa Cruz Biotechnology	SC-739
alkaline phosphatase-conjugated goat anti-mouse antibody	Santa Cruz Biotechnology	SC-204
HRP-conjugated goat anti-rat secondary antibody	Santa Cruz Biotechnology	SC-203
anti-MBP antibody	NEB	E8032S
Chemicals, Peptides, and Recombinant Proteins		
Gelrite	Sigma	G1910
MS	Caisson	MSP01
His6-HA-FERecd-His6	This study	N/A
His6-HA-MALA-His6	This study	N/A
His6-HA-MALB-His6	This study	N/A
His6-HA-BAK1	This study	N/A
MBP-FERecd	This study	N/A
MBP-MALA	This study	N/A
MBP-MALB	This study	N/A
MBP-ANX1ecd	This study	N/A
MBP-ANX2ecd	This study	N/A
MBP-BUPS1ecd	This study	N/A
MBP-WAK1ecd	This study	N/A
Experimental Models: Organisms/Strains		
fer-4	ABRC	GABI_
llg1-1	ABRC	CS6610
llg1-2	ABRC	CS6610
fer-2	Dr. Paul Larsen [21]	N/A
xxt1	ABRC	CS6783
xxt2	ABRC	CS6781
xxt1,2	ABRC	CS1634
mur1-1	ABRC	CS6243
mur1-2	ABRC	CS6244
sos1-1	[29]	N/A
sos2-2	[51]	N/A
RALF1 RNAi in Col-0	Dr. Daniel Moura [24]	N/A

REAGENT or RESOURCE	SOURCE	IDENT
35S::RALF1 in Col-0	Dr. Daniel Moura [24]	N/A
35S::YC3.6 in Col-0	Dr. Gabriele Monshausen [17]	N/A
35S::YC3.6 in *fer-4*	Dr. Gabriele Monshausen [17], this study	N/A
35S::LTI6-YFP in Col-0	Dr. David Ehrhardt [25]	N/A
35S::LTI6-YFP in *fer-4*	This study	N/A
35S::LTI6-YFP in *sos1-1*	This study	N/A
35S::LTI6-YFP in *sos2-2*	This study	N/A
pFER::FER-GFP in *fer-4*	This study	N/A
Oligonucleotides		
Primer pFER-GG-F: GCTCTTCGAGTAGAAAAGTTAAGAGTGGGAACTGGGAAG	This study	N/A
Primer pFER-GG-R: GCTCTTCGCAGCGATCAAGAGCACTTCTCCGGGA	This study	N/A
Primer gFER-GG-F: GCTCTTCACTGATGAAGATCACAGAGGGACGATT	This study	N/A
Primer gFER-GG-R: GCTCTTCACGCACGTCCCTTTGGATTCATGATC	This study	N/A
Recombinant DNA		
pMCY2	[52]	N/A
pFER::FER-GFP	This study	N/A
pMAL-cx5	New England Biolab	N8108
Software and Algorithms		
ImageJ	https://imagej.nih.gov/ij/download.html	N/A
LAS software	Leica	N/A
LAS-X software	Leica	N/A
SlideBook software	Intelligent Imaging Innovations	N/A
Metafluor software	Molecular devices	N/A
MorphographX	http://www.morphographx.org	N/A
Imaris	Bitplane	N/A
JPK Data Processing software	JPK Instruments AG	N/A
MATLAB	https://www.mathworks.com/products/matlab.html	N/A

CONTACT FOR REAGENT AND RESOURCE SHARING

Further information and requests for resources and reagents should be directed to and will be fulfilled by the Lead Contact, José R. Dinneny (dinneny@stanford.edu).

EXPERIMENTAL MODEL AND SUBJECT DETAILS

Seeds of wild-type *Arabidopsis* and T-DNA insertion mutants *fer-4* (GABI_106A06 [20]), *llg1-1*, and *llg1-2* (CS66105 and CS66106 [30]) were obtained from the *Arabidopsis* Biological Research Center (ABRC). *fer-2* seeds were obtained from Dr. Paul Larsen [21]. Mutants *xxt1*(CS67834), *xxt2*(CS67835), *xxt1,2* (CS16349) [36], *mur1-1* (CS6243) and *mur1-2* (CS6244) [50] were also obtained from the ABRC. *sos1-1* and *sos2-2* mutants are as described [29, 51]. Seeds from homozygous T3 plants expressing *RALF1* RNAi construct (irAtRALF1) and *35S::RALF1* were provided by Dr. Tabata Bergonci and Dr. Daniel Moura

[24]. The *35S::YC3.6*-expressing Col-0, *fer-4* T3 seeds were provided by Dr. Gabriele Monshausen (Penn State) [17]. To eliminate position effects of the reporter T-DNA insertion site, *35S::YC3.6*-expressing Col-0 was crossed to *fer-4*. F3-generation seedlings homozygous for the *YC3.6* transgene were used for fluorescence imaging. The plasma-membrane marker line *LTI6-YFP* [25] in Col-0 background was obtained from Dr. David Ehrhardt (Carnegie Institution for Science) and crossed into *fer-4*, *sos1-1*, and *sos2-2* background to generate homozygous *fer-4*, *sos1-1*, and *sos2-2* plants expressing *LTI6-YFP*. To generate *FER* complemented lines, a wild-type version of *FER* including 1.3kb of its native promoter was cloned, ligated with *GFP* at its 3′ and a modified dpGreen-based binary vector, which contained a 35S:PM-mCherry selection marker using Golden Gate Cloning strategy [52]. The construct was introduced to *fer-4* plants through agrobacterium-based transformation using floral dip method. Plants from two independent GFP-expressing homozygous T3 lines were used for this study.

METHOD DETAILS

Plant growth conditions—Surface-sterilized *Arabidopsis thaliana* (Col-0) seeds were plated on 0.7% gellan gum (Gelrite, Sigma G1910) containing 4.33 g/L Murashige and Skoog salts (Caisson MSP01-50LT) and 1% sucrose, pH 5.7, stratified for 2 d at 4°C and grown in a Percival CU41L4 incubator at a constant temperature of 22°C with long-day conditions (16 h light and 8 h dark). Seedlings were grown for 5 d before being transferred to media supplemented with NaCl or other chemicals. To prepare media for different chemical treatment, chemicals were added to the MS media to their final concentrations before adjusting pH.

For short-term imaging of intracellular cytosolic [Ca^{2+}] levels, surface-sterilized *Arabidopsis thaliana* (Col-0) seeds were plated on 0.8% Agar (Duchefa, Netherlands) containing 0.5X strength Murashige and Skoog salts (Duchefa, Netherlands), pH 5.8, stratified for 2 d at 4°C and grown in a Percival CU41L4 incubator at a constant temperature of 22°C with long-day conditions (16 h light and 8 h dark) at 120–150 μmol m^{-2} s^{-1} light intensity for five days.

Root growth analysis—For end-point analysis of root length, seedlings were grown on standard media for 5 d then transferred to media supplemented with various concentration of NaCl, mannitol or sorbitol, position of root tips marked on the plate and grown for 1 d. Images were captured using a CanonScan 9000F flatbed scanner (Canon). The change in root length was quantified using ImageJ.

For live-imaging analysis of primary root growth, 5-d-old seedlings were transferred to media supplemented with 140 mM NaCl and imaged using a custom macroscopic imaging system as previously described [53]. Growth rates were quantified using a semi-automated image analysis algorithm, RootTip Trace, written as a plugin for ImageJ as previously described [3]. In brief, a line along the midline of the root from the tip to the base was drawn in the last frame of a stack of time-lapse images. The algorithm would calculate the elongation of the root along the line in each frame. Growth measurements made during 1 h were summed together to calculate hourly growth rate.

Fluorescence microscopy—Imaging chambers were made from a cut-open 60 × 15-mm Petri dish (Fisher, AS4052) with a 22 × 40 (mm) No. 1.5 micro cover glasses (VWR, 48393-172) taped to the bottom. Seedlings were transferred to the center of the chamber with the roots sandwiched between the cover glass and a 0.5-cm-thick slab of gelrite media with appropriate supplements. Water-soaked kimwipes were places around the edge of the chamber to maintain humidity and the chamber was sealed with Parafilm.

Bright-field images were taken from a Leica DMI6000 inverted compound microscope with HC PL APO 10× / 0.4 CS objective (Leica) and LAS software (Leica).

For long-term 4D confocal imaging, roots of LTI6-YFP-expressing seedlings were imaged on a Leica TCS SP8 microscope with an HC PL APO 20× / 0.75 n.a. objective. A super-continuum white light laser was tuned to 515 nm for excitation. Emission was detected from 525 to 575 nm by a HyD SMD detector. Imaging data were acquired using LAS-X software (Leica).

For long-term imaging of intracellular cytosolic [Ca^{2+}], roots of YC3.6-expressing seedlings were imaged on an inverted epifluorescence microscope (Leica DM IRE2). The objective used was an HC PL APO 10× / 0.4 n.a. (Leica). A Sutter Lambda illumination system was used for excitation. CFP/FRET was excited at 102 μW for 200 ms using a xenon lamp and a Chroma ET 436/20 emission filter. Control YFP was excited at 149 μW for 100 ms using a Chroma ET 500/20 emission filter. CFP and YFP emissions were detected through ET470/22 and ET550/49 filters respectively. Imaging data were acquired using SlideBook software (Intelligent Imaging Innovations).

Short-term imaging of intracellular cytosolic [Ca^{2+}] levels was performed in a custom-made flow-through chamber as previously described [54]. For NaCl or mannitol treatment, the seedlings were washed with incubation buffer (5 mM KCl, 50 μM $CaCl_2$, 10 mM MES, pH 5.8 adjusted with TRIS) for 3 min by continuous circulation (1.5 mL min^{-1}) by a peristaltic pump. Then the incubation buffer was exchanged with buffer (5 mM KCl, 50 μM $CaCl_2$, 10 mM MES, pH 5.8 adjusted with TRIS) supplemented with 150 mM NaCl or 300 mM mannitol. In this setup, buffer exchange in the flow-through chamber occurs at 54 s after valve activation for initiation of buffer exchange. After 7 min treatment, seedlings were washed with incubation buffer. An inverted ZEISS Axio observer (Carl Zeiss Microimaging, Goettingen, Germany) equipped with an emission filter wheel (LUDL Electronic Products, Hawthorne, NY, USA) and a Photometrics cool SNAPHQ2 CCD camera (Tucson, Arizona) with a Zeiss EC Plan-NEOFLUAR 5×/0.16 dry objective was used for imaging. A xenon short arc reflector lamp (Hamamatsu) through a 440 nm filter was used to excite the CFP of YC3.6. For emission detection, 485 nm (CFP) and 535 nm (YFP) emission filters were used. CFP and YFP (FRET) Images were obtained with Metafluor software (Meta Imaging series 7.7 from Molecular devices). An exposure time of 300 ms was used for both CFP and YFP (FRET) image acquisition with binning 2.

MorphographX analysis—MorphographX analysis is performed according to the user manual [26] with some modifications. LTI6-YFP image stacks were filtered using Gaussian Blur with a radius of 0.3 μm. “Edge Detect” was used to extract the root shape with a

threshold between 300 and 600 followed by “Fill Holes” to follow the raw signal as closely as possible. A mesh was generated using the “Marching Cubes Surface” with a cube size of 5 μm. The mesh was trimmed at the bottom and subsequently smoothed 5 times by “Smooth Mesh” and refined 2 times by performing the “Subdivide the Mesh” function. The LTI6-YFP signal was projected onto the mesh. Root epidermal cells were identified by manual seeding using “Add New Seed” tool and the mesh was segmented using a “Watershed Segmentation” algorithm. Same cells in a time series imaging were associated and labeled with the same color using “Parent labeling.”

Quantification of cell bursting and volume change—4D confocal imaging data of roots expressing LTI6-YFP were 3D reconstructed and segmented to hourly movies using ImageJ. Events that cells loss shape and YFP signal were counted manually in the root epidermal and cortical layers. For comparing cell death between WT, *fer*, and *sos* mutants, single plane LTI6-YFP images were aligned to the root tip using the “StackReg” plugin and reoriented using the “Rotate” function. A 750 μm region of the root tip was divided into 10 sections for analysis. Single cell death events were counted as a loss in LTI6-YFP signal. Due to the large number of cells in the lateral root cap and meristematic region, a total number of cell in the first three sections from the tip were estimated to be 25, 60, 60. For cell volume measurement, 4D confocal image series of roots expressing LTI6-YFP were pre-processed (rolling ball background subtraction 50, Gaussian blur 1–2) in ImageJ. Cell segmentation and volumetric analysis was performed in the Cell module of Imaris (Bitplane). For counting cell bursting events using bright-field images, events that cause root cells to rapidly lose volume or appear opaque were quantified as a cell death event.

Atomic force microscopy—The AFM data were collected as previously described [31, 55]. Roots were immobilized on glass slides and surrounded by stiff agarose after dissection. Approximate elongation zone was defined based on the visual landmark observed through a bright field microscope. To measure wall properties at normal turgor pressure, the roots were immersed in water with or without salts (140 mM NaCl). In order to extract the mechanical properties of only the outer cell wall, the maximum indentation force was set for a maximum indentation of 60 nM. The following cantilever was used: “Nano World” (Nanosensors Headquarters, Neuchâtel, Switzerland) SD-R150-T3L450B tips with a spring constant of 0.15–1.83N/m (the one used was estimated to be 0.85 N/m) with silicon point probe tips of a 150-nm radius.

All force spectroscopy experiments were performed as previously described [31, 55]. Briefly, stiffness of samples was determined as follows: an AFM cantilever loaded with a spherical tip was used to indent the sample over a 40 × 100 μm square area, within the area 20 × 50 measurements were made resulting in 1000 force-indentation experiments; each force-indentation experiment was treated with a Hertzian indentation model to extract the apparent Young’s modulus (E_A); each pixel in a stiffness map represents the apparent Young’s modulus from one force-indentation point. The E_A was calculated using the JPK Data Processing software (ver. Spm - 4.0.23, JPK Instruments AG, Germany), which allows for a more standardized analysis than the estimation of the E_A using a standard Hertzian contact model [31, 55]. Only the retraction curve was used in our analyses as is typically the

case in nano-indentation experiments. Similar stiffness differences were also observed when using the deformation curve (data not shown), yet this measurement appeared more sensitive to the topography leading to aberrant measurements in particular on growing root hairs. The best fit was obtained using a Hertzian model with 50 nm as tip radius. A Poisson ratio of 0.5 was assumed for the material. Range distribution of E_A from 4 kPas to 100 kPas in 1-kPa binned groups was calculated using MATLAB.

Recombinant protein production and purification—His_6-HA- or MBP-tagged FER extracellular domain (FERecd), MALA or MALB domains were expressed either in insect cell (Tn5, Invitrogen) or *E. coli* (BL21) based on standard procedure provided by Invitrogen. For protein isolation, insect cell medium was buffer-exchanged and concentrated into Ni^{2+} binding buffer (50 mM sodium phosphate buffer pH 7.2, 250 mM NaCl with 40 mM imidazole). The samples were loaded onto Ni^{2+}-Sepharose FF column (GE Healthcare) and eluted with an imidazole gradient of 40–400 mM imidazole. His_6-HA-FERecd-His_6 protein, referred to as HA-FERecd, eluted at approximately 300 mM imidazole as a single Coomassie Blue-stained band with a faint smear after SDS-PAGE, most probably due to glycosylation. It was then buffer-exchanged into 25 mM Tris-HCl pH 7.5, 100 mM NaCl and concentrated to 0.5 mg/mL and stored at 4°C for use in pectin-binding experiments within two to three days. Antibodies against the HA tag were used to detect bound HA-FERecd.

The pMAL-cx5 vector (New England Biolab) was used to express in BL21 *E. coli* the following proteins: MBP, MBP-FERecd, MBP-MALA, MBP-MALB, MBP-ANX1ecd, MBP-ANX2ecd, MBP-BUPS1ecd and MBP-WAK1ecd. They were purified by affinity chromatography on amylose resin by standard methods as previously described [20]. Briefly, cells were resuspended in binding buffer [40 mM Tris-HCl (pH 7.5), 100 mM NaCl, 1 mM Na_2-EDTA] and sonicated with six 10 s pulses at 1-min intervals. After removal of cell debris by centrifugation at 4°C, proteins were applied to amylose resin (NEB) in the same binding buffer. GFP-His_6 was purified by elution from Talon metal affinity chromatography (Clontech) by imidazole. His_6-HA-BAK1ecd was affinity-purified from Talon resin.

Analysis of protein interaction with pectin—Pectin interaction with FERecd, MALA and MALB were examined by five different assay methods to detect FER-pectin interactions: (1) in-gel affinity electrophoresis, (2) protein-pectin interaction followed by electrophoretic mobility shift assay, (3) two dot-blot assays one with immobilized proteins and one with immobilized pectin, (4) a bead based pull-down assay with protein immobilized on amylose beads, and (5) ELISA. Interactions were based on immunodetection using either monoclonal antibodies, JIM5 or M38 (CCRC or gift from Paul Knox), against pectin [20, 49], or anti-HA, anti-His_6 or anti-MBL antibodies against the protein tags. All procedures were carried out at room temperature unless otherwise indicated.

Affinity electrophoresis assays were modeled after previous protein-carbohydrate interaction studies [56]. Briefly, HA-FERecd (2 mg) were electrophoresed in one well of individual 6% native polyacrylamide gels (26:1, acrylamide: bisacrylamide) in a 30 mM MES/30 mM histidine (His) buffer, pH 6.1, each polymerized with different concentrations (0 to 0.5

mg/mL) of PGA (Sigma). Similarly electrophoresed BSA (5 mg) served as controls. Gels run with BSA were stained directly with Coomassie blue. Gels run with HA-FERecd were first soaked in 25 mM Tris-HCl pH 7.5 and 0.1% SDS for 30 min and then transferred to PVDF for immune-detection using mouse anti-HA antibody (Santa Cruz; 1: 5000), followed by incubation with alkaline phosphatase-conjugated goat anti-mouse antibody (Santa Cruz; 1:5000), and developed in alkaline phosphatase developing buffer (20 mM Tris-HCl pH 9.5, 100 mM NaCl, 10 mM $MgCl_2$) in the presence of NBT and BCIP.

Electrophoretic mobility shift assays were modeled after standard gel-shift assays for protein-nucleic acid interaction on native PAGE. HA-FERecd or control BSA were incubated with increasing concentrations of PGA for 15 min prior to gel loading. Running buffer, electrophoretic conditions, protein transfer and detection were the same as those described above for affinity electrophoresis.

For ELISA, 4 μg of HA-FERecd or control proteins were coated on 96-well microtiter plates in coating buffer (25 mM Tris-HCl pH 8, 60 mM NaCl) for 2 h at room temperature. The coated plates were washed in TBST (25 mM Tris-HCl pH 7.5, 100 mM NaCl, 0.05% Tween20), blocked with 2% BSA in TBST for 2 h, and washed in binding buffer (25 mM Bis-Tris-HCl pH 6.5, 100 mM NaCl) before incubation with 0, 1, 2, or 5 mg/mL PGA in binding buffer for 2 h. The plates were washed and then probed for PGA with JIM5 antibody (at 1:1000 dilution) overnight at 4°C. After washing, the plates were probed with (HRP)-conjugated goat anti-rat secondary antibody (Santa Cruz) at 1:5000 dilution for 1 hr, washed and developed with the colorimetric peroxidase substrate o-phenylenediamine dihydrochloride (OPD) in 50 mM citric acid, 50 mM sodium phosphate, pH 5, for 20 min. Absorbance at A450 (A450) was measured on a SpectraMax M5 Multi-Mode Microplate Reader (Molecular Devices) to quantify protein-PGA interaction.

Dot blot assays were either based on proteins (0.25 μg of target HA-FERecd, or controls proteins, GFP-His_6, or MBP) immobilized onto PVDF membranes (Perkin-Elmer) or heat-fragmented PGA immobilized onto nitrocellulose membrane (BA85 S&S Protran). Membranes with immobilized proteins were blocked in 2% BSA in TBS (25 mM Tris-HCl pH 7.5, 100 mM NaCl) for 1 h and were then washed in binding buffer (25 mM Bis-Tris-HCl pH 6.5, 100 mM NaCl). They were then incubated with 0, 0.1, 0.5, and 1 mg/mL PGA in binding buffer for 1.5 h, followed by three washes in binding buffer, and three washes in TBST for at least 15 min each. The blots were then incubated with JIM5 antibody (1:1000 dilution), then with horseradish peroxidase (HRP)-conjugated goat anti-rat secondary antibody (Santa Cruz; 1:5000 dilution), with five washes in TBST between each step. Bound PGA was detected by chemiluminescence in standard developing buffer (100 mM Tris-HCl pH 8.5, 85 mM p-coumaric acid, 250 mM luminol, 0.0034% H_2O_2).

For dot blot assays with immobilized pectin, dots of 1.5 μL of PGA at varying concentrations of PGA serially diluted from 20 mg/mL stocks were spotted onto the membrane and allowed to dry. Quantity of PGA in each dot is as indicated in the figures. The pectin dot blots were blocked, incubated with purified recombinant MBP or fusion proteins at 4°C for 2 h (at concentrations indicated in figures or figure legends), and then with anti-MBP antibody (NEB) for 1 h with three to five washes in between. After rinsing,

the filters were either incubated with alkaline phosphatase-conjugated goat anti-rabbit IgG antibody (Santa Cruz) or for 1 h for colorimetric detection in alkaline phosphatase developing buffer or with anti-MBP-HRP (1:10000 dilution, 1 mg/mL), followed by chemiluminescence detection of bound proteins. Signal quantification was carried out using ImageJ. Pectin immobilized on nitrocellulose membrane was used for binding assays with all other proteins tested. For these dot blot assays, every binding was carried out in triplicate samples, ad each binding assay was repeated at least three times, using independently prepared protein preparations.

For assays with protein immobilized on amylose resin, MALA-MBP or MBP were coated on resin as for affinity chromatography. After washing, the protein-coated resins were incubated with PGA (2 mg/mL, sonicated) for 2 h or overnight. After wash, the resins were incubated with JIM5 (1:500) or M38 (1:100) antibody, followed by FITC-labeled secondary antibody to detect bound pectin microscopically by immunofluorescence. The input protein on the coated beads was detected by anti-MBP antibody (1:500).

[Ca^{2+}] image processing—For the calculation of the change in [Ca^{2+}] concentration over time, the FRET/CFP ratio images were recalculated from the CFP and FRET images with ImageJ software. Normalized change in ratio values (Rt-R0): R0 (abbreviated as ΔR: R0) was calculated, where Rt is the ratio at time point t and R0 is the basal ratio value. A [Ca^{2+}] spike is defined as an event with local [Ca^{2+}] increase of ΔR: R0 > 0.2. A size minimum of 3 pixels was used to exclude sporadic signals.

Kinematic analysis of growth rate—Kinematic analysis was performed using the control YFP images taken at the same time as the FRET and CFP images used for calculating changes in [Ca^{2+}] concentration. Time series of images were opened in ImageJ and aligned to the root tip using the “StackReg” Plugin and reoriented using the “Rotate” function so that the roots were vertical. The tip 600 μm (360 pixels) region was selected for analysis. To calculate elemental growth rate, a kymograph was created by drawing a 1 × 360 pixel box near the midline of the root and performing the “Montage” function with the whole image stack. The kymographs were subsequently gridded into 30 × 12 rectangles where each column corresponded to a 30-min time window and each row representing a 50-μm size region of the root tip. Points were marked where cell boundary lines intercept with the vertical grid lines in each rectangle and elemental growth rate was calculated by dividing the difference in Y axes with time and zone size: (y2-y1) μm /0.5hr * 50 μm.

QUANTIFICATION AND STATISTICAL ANALYSIS

For root growth analysis, all experiment were performed at least three times. Sample size, n, for each experiment are given in the figure legends. For AFM, microscopy and immunolabeling, all experiments were performed at least three times using independent biological samples with similar results being observed. Statistical comparisons (Two-way ANOVA or Student’s t test) were conducted with R software.

Supplementary Material

Refer to Web version on PubMed Central for supplementary material.

Acknowledgments

We thank David Ehrhardt, Zhiyong Wang, and members of the Dinneny lab for their discussions and helpful comments during the preparation ofthismanuscript. The AFM experiment was supported by the Sainsbury Laboratory, Cambridge University. Funding was providedby grantsfrom the National Science Foundation (NSF) Plant Genome Research Program (IOS 1238202), NIH NIGMS (R01 GM123259-01), and Carnegie Institution for Science Endowment to J.R.D.; grants from the NSF (IOS-1146941, IOS-1147165, IOS-1645854) to A.Y.C. and H.-M.W.; and a grant from the German Research Foundation (Ku 931/14-1) to J.K. The research of J.R.D. was supported in part by a Faculty Scholar grant from the Howard Hughes Medical Institute and the Simons Foundation.

References

1. Robbins NE 2nd, Dinneny JR. The divining root: moisture-driven responses of roots at the micro- and macro-scale. J Exp Bot. 2015; 66:2145–2154. [PubMed: 25617469]
2. Zhu JK. Salt and drought stress signal transduction in plants. Annu Rev Plant Biol. 2002; 53:247–273. [PubMed: 12221975]
3. Geng Y, Wu R, Wee CW, Xie F, Wei X, Chan PMY, Tham C, Duan L, Dinneny JR. A spatio-temporal understanding of growth regulation during the salt stress response in *Arabidopsis*. Plant Cell. 2013; 25:2132–2154. [PubMed: 23898029]
4. Galvan-Ampudia CS, Julkowska MM, Darwish E, Gandullo J, Korver RA, Brunoud G, Haring MA, Munnik T, Vernoux T, Testerink C. Halotropism is a response of plant roots to avoid a saline environment. Curr Biol. 2013; 23:2044–2050. [PubMed: 24094855]
5. Dinneny JR, Long TA, Wang JY, Jung JW, Mace D, Pointer S, Barron C, Brady SM, Schiefelbein J, Benfey PN. Cell identity mediates the response of *Arabidopsis* roots to abiotic stress. Science. 2008; 320:942–945. [PubMed: 18436742]
6. Scheible WR, Eshed R, Richmond T, Delmer D, Somerville C. Modifications of cellulose synthase confer resistance to isoxaben and thiazolidinone herbicides in *Arabidopsis* Ixr1 mutants. Proc Natl Acad Sci USA. 2001; 98:10079–10084. [PubMed: 11517344]
7. Arioli T, Peng L, Betzner AS, Burn J, Wittke W, Herth W, Camilleri C, Höfte H, Plazinski J, Birch R, et al. Molecular analysis of cellulose biosynthesis in *Arabidopsis*. Science. 1998; 279:717–720. [PubMed: 9445479]
8. Kang JS, Frank J, Kang CH, Kajiura H, Vikram M, Ueda A, Kim S, Bahk JD, Triplett B, Fujiyama K, et al. Salt tolerance of *Arabidopsis thaliana* requires maturation of *N*-glycosylated proteins in the Golgi apparatus. Proc Natl Acad Sci USA. 2008; 105:5933–5938. [PubMed: 18408158]
9. Voxeur A, Höfte H. Cell wall integrity signaling in plants: “to grow or not to grow that’s the question. Glycobiology. 2016; 26:950–960. [PubMed: 26945038]
10. Hématy K, Sado PE, Van Tuinen A, Rochange S, Desnos T, Balzergue S, Pelletier S, Renou JP, Höfte H. A receptor-like kinase mediates the response of *Arabidopsis* cells to the inhibition of cellulose synthesis. Curr Biol. 2007; 17:922–931. [PubMed: 17540573]
11. Miyazaki S, Murata T, Sakurai-Ozato N, Kubo M, Demura T, Fukuda H, Hasebe M. ANXUR1 and 2, sister genes to FERONIA/SIRENE, are male factors for coordinated fertilization. Curr Biol. 2009; 19:1327–1331. [PubMed: 19646876]
12. Van der Does D, Boutrot F, Engelsdorf T, Rhodes J, McKenna JF, Vernhettes S, Koevoets I, Tintor N, Veerabagu M, Miedes E, et al. The *Arabidopsis* leucine-rich repeat receptor kinase MIK2/LRR-KISS connects cell wall integrity sensing, root growth and response to abiotic and biotic stresses. PLoS Genet. 2017; 13:e1006832. [PubMed: 28604776]
13. Li C, Wu HM, Cheung AY. FERONIA and her pals: functions and mechanisms. Plant Physiol. 2016; 171:2379–2392. [PubMed: 27342308]
14. Lindner H, Müller LM, Boisson-Dernier A, Grossniklaus U. CrRLK1L receptor-like kinases: not just another brick in the wall. Curr Opin Plant Biol. 2012; 15:659–669. [PubMed: 22884521]
15. Rotman N, Rozier F, Boavida L, Dumas C, Berger F, Faure JE. Female control of male gamete delivery during fertilization in *Arabidopsis thaliana*. Curr Biol. 2003; 13:432–436. [PubMed: 12620194]

16. Huck N, Moore JM, Federer M, Grossniklaus U. The *Arabidopsis* mutant feronia disrupts the female gametophytic control of pollen tube reception. Development. 2003; 130:2149–2159. [PubMed: 12668629]
17. Shih HW, Miller ND, Dai C, Spalding EP, Monshausen GB. The receptor-like kinase FERONIA is required for mechanical signal transduction in *Arabidopsis* seedlings. Curr Biol. 2014; 24:1887–1892. [PubMed: 25127214]
18. Ngo QA, Vogler H, Lituiev DS, Nestorova A, Grossniklaus U. A calcium dialog mediated by the FERONIA signal transduction pathway controls plant sperm delivery. Dev Cell. 2014; 29:491–500. [PubMed: 24814317]
19. Duan Q, Kita D, Johnson EA, Aggarwal M, Gates L, Wu HM, Cheung AY. Reactive oxygen species mediate pollen tube rupture to release sperm for fertilization in *Arabidopsis*. Nat Commun. 2014; 5:3129. [PubMed: 24451849]
20. Duan Q, Kita D, Li C, Cheung AY, Wu HM. FERONIA receptor-like kinase regulates RHO GTPase signaling of root hair development. Proc Natl Acad Sci USA. 2010; 107:17821–17826. [PubMed: 20876100]
21. Deslauriers SD, Larsen PB. FERONIA is a key modulator of brassinosteroid and ethylene responsiveness in *Arabidopsis* hypocotyls. Mol Plant. 2010; 3:626–640. [PubMed: 20400488]
22. Chen J, Yu F, Liu Y, Du C, Li X, Zhu S, Wang X, Lan W, Rodriguez PL, Liu X, et al. FERONIA interacts with ABI2-type phosphatases to facilitate signaling cross-talk between abscisic acid and RALF peptide in *Arabidopsis*. Proc Natl Acad Sci USA. 2016; 113:E5519–E5527. [PubMed: 27566404]
23. Haruta M, Sabat G, Stecker K, Minkoff BB, Sussman MR. A peptide hormone and its receptor protein kinase regulate plant cell expansion. Science. 2014; 343:408–411. [PubMed: 24458638]
24. Bergonci T, Ribeiro B, Ceciliato PHO, Guerrero-Abad JC, Silva-Filho MC, Moura DS. *Arabidopsis thaliana* RALF1 opposes brassinosteroid effects on root cell elongation and lateral root formation. J Exp Bot. 2014; 65:2219–2230. [PubMed: 24620000]
25. Cutler SR, Ehrhardt DW, Griffitts JS, Somerville CR. Random GFP:cDNA fusions enable visualization of subcellular structures in cells of *Arabidopsis* at a high frequency. Proc Natl Acad Sci USA. 2000; 97:3718–3723. [PubMed: 10737809]
26. Barbier de Reuille P, Routier-Kierzkowska AL, Kierzkowski D, Bassel GW, Schüpbach T, Tauriello G, Bajpai N, Strauss S, Weber A, Kiss A, et al. MorphoGraphX: a platform for quantifying morphogenesis in 4D. eLife. 2015; 4:05864. [PubMed: 25946108]
27. Shi H, Ishitani M, Kim C, Zhu JK. The *Arabidopsis thaliana* salt tolerance gene SOS1 encodes a putative Na^+/H^+ antiporter. Proc Natl Acad Sci USA. 2000; 97:6896–6901. [PubMed: 10823923]
28. Liu J, Ishitani M, Halfter U, Kim CS, Zhu JK. The *Arabidopsis thaliana* SOS2 gene encodes a protein kinase that is required for salt tolerance. Proc Natl Acad Sci USA. 2000; 97:3730–3734. [PubMed: 10725382]
29. Zhu JK, Liu J, Xiong L. Genetic analysis of salt tolerance in *Arabidopsis*. Evidence for a critical role of potassium nutrition. Plant Cell. 1998; 10:1181–1191. [PubMed: 9668136]
30. Li C, Yeh FL, Cheung AY, Duan Q, Kita D, Liu MC, Maman J, Luu EJ, Wu BW, Gates L, et al. Glycosylphosphatidylinositol-anchored proteins as chaperones and co-receptors for FERONIA receptor kinase signaling in *Arabidopsis*. eLife. 2015; 4:e06587.
31. Peaucelle A. AFM-based mapping of the elastic properties of cell walls: at tissue, cellular, and subcellular resolutions. J Vis Exp. 2014:51317.
32. Peaucelle A, Braybrook S, Höfte H. Cell wall mechanics and growth control in plants: the role of pectins revisited. Front Plant Sci. 2012; 3:121. [PubMed: 22685449]
33. Munarin F, Tanzi MC, Petrini P. Advances in biomedical applications of pectin gels. Int J Biol Macromol. 2012; 51:681–689. [PubMed: 22776748]
34. O'Neill MA, Ishii T, Albersheim P, Darvill AG. Rhamnogalacturonan II: structure and function of a borate cross-linked cell wall pectic polysaccharide. Annu Rev Plant Biol. 2004; 55:109–139. [PubMed: 15377216]
35. O'Neill MA, Eberhard S, Albersheim P, Darvill AG. Requirement of borate cross-linking of cell wall rhamnogalacturonan II for *Arabidopsis* growth. Science. 2001; 294:846–849. [PubMed: 11679668]

36. Cavalier DM, Lerouxel O, Neumetzler L, Yamauchi K, Reinecke A, Freshour G, Zabotina OA, Hahn MG, Burgert I, Pauly M, et al. Disrupting two *Arabidopsis thaliana* xylosyltransferase genes results in plants deficient in xyloglucan, a major primary cell wall component. Plant Cell. 2008; 20:1519–1537. [PubMed: 18544630]
37. Boisson-Dernier A, Kessler SA, Grossniklaus U. The walls have ears: the role of plant CrRLK1Ls in sensing and transducing extracellular signals. J Exp Bot. 2011; 62:1581–1591. [PubMed: 21252257]
38. Ge Z, Bergonci T, Zhao Y, Zou Y, Du S, Liu MC, Luo X, Ruan H, García-Valencia LE, Zhong S, et al. *Arabidopsis* pollen tube integrity and sperm release are regulated by RALF-mediated signaling. Science. 2017; 358:1596–1600. [PubMed: 29242234]
39. Decreux A, Messiaen J. Wall-associated kinase WAK1 interacts with cell wall pectins in a calcium-induced conformation. Plant Cell Physiol. 2005; 46:268–278. [PubMed: 15769808]
40. Sun Y, Han Z, Tang J, Hu Z, Chai C, Zhou B, Chai J. Structure reveals that BAK1 as a co-receptor recognizes the BRI1-bound brassinolide. Cell Res. 2013; 23:1326–1329. [PubMed: 24126715]
41. Nagai T, Yamada S, Tominaga T, Ichikawa M, Miyawaki A. Expanded dynamic range of fluorescent indicators for Ca(2+) by circularly permuted yellow fluorescent proteins. Proc Natl Acad Sci USA. 2004; 101:10554–10559. [PubMed: 15247428]
42. Bosch M, Hepler PK. Pectin methylesterases and pectin dynamics in pollen tubes. Plant Cell. 2005; 17:3219–3226. [PubMed: 16322606]
43. Kohorn BD, Kohorn SL. The cell wall-associated kinases, WAKs, as pectin receptors. Front Plant Sci. 2012; 3:88. [PubMed: 22639672]
44. Sinclair SA, Larue C, Bonk L, Khan A, Castillo-Michel H, Stein RJ, Grolimund D, Begerow D, Neumann U, Haydon MJ, Krämer U. Etiolated seedling development requires repression of photomor-phogenesis by a small cell-wall-derived dark signal. Curr Biol. 2017; 27:3403–3418. e7. [PubMed: 29103938]
45. Olsen JL, Rouzé P, Verhelst B, Lin YC, Bayer T, Collen J, Dattolo E, De Paoli E, Dittami S, Maumus F, et al. The genome of the seagrass *Zostera marina* reveals angiosperm adaptation to the sea. Nature. 2016; 530:331–335. [PubMed: 26814964]
46. Stegmann M, Monaghan J, Smakowska-Luzan E, Rovenich H, Lehner A, Holton N, Belkhadir Y, Zipfel C. The receptor kinase FER is a RALF-regulated scaffold controlling plant immune signaling. Science. 2017; 355:287–289. [PubMed: 28104890]
47. Espinoza C, Liang Y, Stacey G. Chitin receptor CERK1 links salt stress and chitin-triggered innate immunity in *Arabidopsis*. Plant J. 2017; 89:984–995. [PubMed: 27888535]
48. Yasuda M, Ishikawa A, Jikumaru Y, Seki M, Umezawa T, Asami T, Maruyama-Nakashita A, Kudo T, Shinozaki K, Yoshida S, Nakashita H. Antagonistic interaction between systemic acquired resistance and the abscisic acid-mediated abiotic stress response in *Arabidopsis*. Plant Cell. 2008; 20:1678–1692. [PubMed: 18586869]
49. Knox JP, Linstead PJ, King J, Cooper C, Roberts K. Pectin esterification is spatially regulated both within cell walls and between developing tissues of root apices. Planta. 1990; 181:512–521. [PubMed: 24196931]
50. Reiter WD, Chapple CCS, Somerville CR. Altered growth and cell walls in a fucose-deficient mutant of *Arabidopsis*. Science. 1993; 261:1032–1035. [PubMed: 17739625]
51. Wu SJ, Ding L, Zhu JK. SOS1, a genetic locus essential for salt tolerance and potassium acquisition. Plant Cell. 1996; 8:617–627. [PubMed: 12239394]
52. Emami S, Yee MC, Dinneny JR. A robust family of Golden Gate *Agrobacterium* vectors for plant synthetic biology. Front Plant Sci. 2013; 4:339. [PubMed: 24032037]
53. Duan L, Dietrich D, Ng CH, Chan PMY, Bhalerao R, Bennett MJ, Dinneny JR. Endodermal ABA signaling promotes lateral root quiescence during salt stress in *Arabidopsis* seedlings. Plant Cell. 2013; 25:324–341. [PubMed: 23341337]
54. Behera S, Wang N, Zhang C, Schmitz-Thom I, Strohkamp S, Schültke S, Hashimoto K, Xiong L, Kudla J. Analyses of Ca^{2+} dynamics using a ubiquitin-10 promoter-driven Yellow Cameleon 3.6 indicator reveal reliable transgene expression and differences in cytoplasmic Ca^{2+} responses in *Arabidopsis* and rice (*Oryza sativa*) roots. New Phytol. 2015; 206:751–760. [PubMed: 25641067]

55. Peaucelle A, Wightman R, Höfte H. The control of growth symmetry breaking in the *Arabidopsis* hypocotyl. Curr Biol. 2015; 25:1746–1752. [PubMed: 26073136]

56. Tomme P, Boraston A, Kormos JM, Warren RA, Kilburn DG. Affinity electrophoresis for the identification and characterization of soluble sugar binding by carbohydrate-binding modules. Enzyme Microb Technol. 2000; 27:453–458. [PubMed: 10978766]

Highlights

- FER is necessary to maintain cell-wall integrity during the salt-stress response
- Pectin cross-linking protects cell walls against damage induced by salinity
- The extracellular domain of FER interacts directly with pectin
- FER induces cell-specific [Ca^{2+}] transients that maintain cell-wall integrity

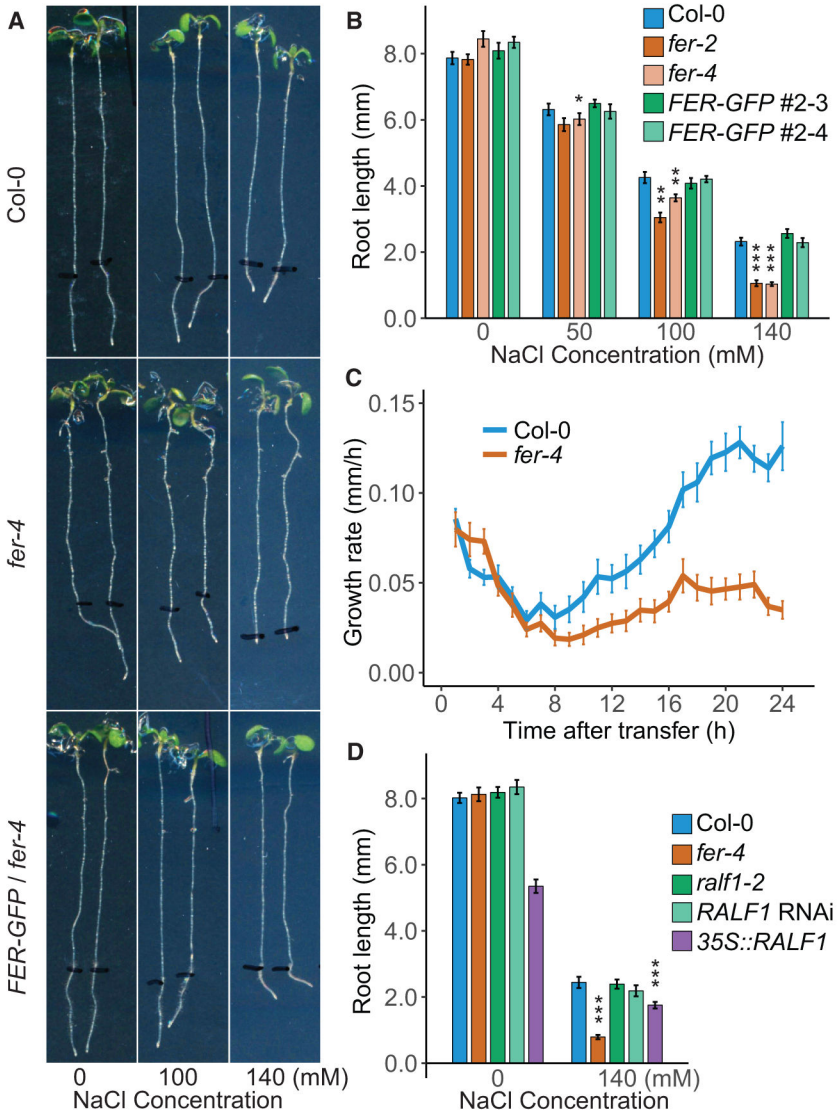

Figure 1. *FER* Is Required for Root Growth Recovery during High Salinity

(A) Seedlings of WT, *fer-4*, and a *FER* complemented line 24 hr after transfer to media. Black lines mark the position of the root tip at time of transfer.

(B) Root growth of WT, two *fer* alleles, and two independent *FER* complemented lines 24 hr after transfer to media. n ≥ 15.

(C) Quantification of hourly growth rate of WT and *fer-4* roots transferred to media containing 140 mM NaCl. n = 16.

(D) Root growth of WT, *fer-4*, *ralf1-2*, *RALF1* RNAi, and *RALF1* overexpression lines 24 hr after transfer to media. n ≥ 17.

Error bars indicate SEM. *p < 0.05, **p < 0.01, ***p < 0.001, two-way ANOVA compared to WT and control treatment. See also Figure S1.

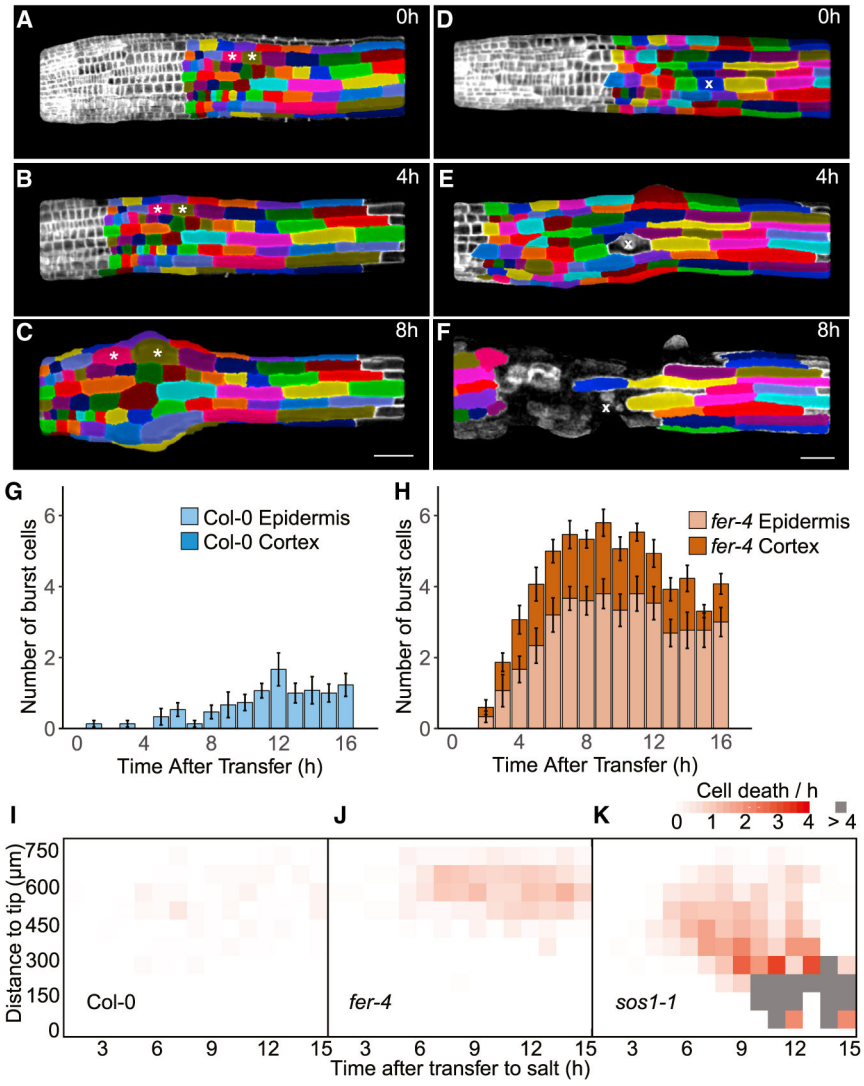

Figure 2. *FER* Maintains Cell Integrity during Growth Recovery after Salt Stress

(A–F) Time-lapse images of LTI6-YFP-expressing WT (A–C) and *fer-4* (D–F) roots after transfer to media containing 140 mM NaCl. Individual epidermal cells at each time point are identified by the same color after image segmentation in MorphoGraphX. Asterisks mark two WT cells that display loss of anisotropy during recovery. "x" marks a *fer* cell that burst during growth. Scale bars, 50 µm.

(G and H) Quantification of burst cells from time-lapse imaging of LTI6-YFP-expressing WT (G) and *fer-4* (H) roots. n = 15.

(I–K) Heatmaps showing the average number of burst cells of WT (I), *fer-4* (J), and *sos1-1* (K) roots in each 750-µm longitudinal zone during each 1-hr time window after transfer to media containing 140 mM NaCl. Quantification is performed with a single Z section, 16 µm from the epidermis. Gray areas indicate average cell death rate higher than 4 per hr. n ≥ 10. Error bars indicate SEM. See also Figures S2 and S3 and Movie S1.

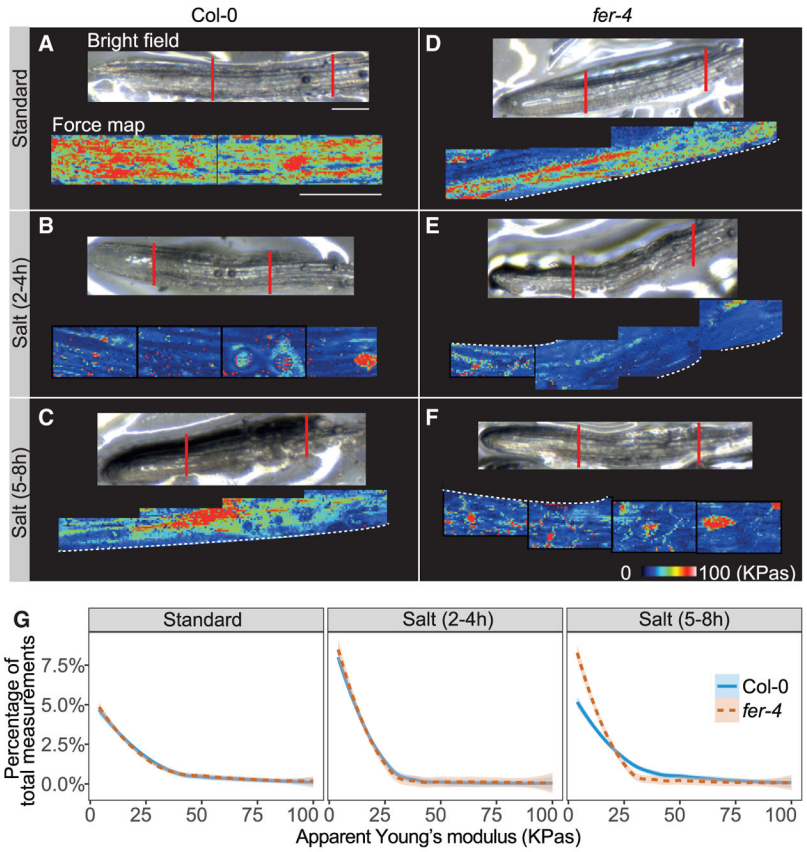

Figure 3. Regulation of Cell-Wall Mechanics Is Impaired in the *fer* Mutant after Salt Treatment

(A–F) Apparent Young's modulus (E_A, or "stiffness") map of WT (A–C) and *fer-4* (D–F) root epidermal cells in the elongation zone. Samples were assayed in control condition (A and D) or 2–4 hr (B and E) and 5–8 hr (C and F) after 140 mM NaCl treatment. Bright-field images show the region where the analysis was performed. Scale bars, 100 μm.

(G) Range distribution of the E_A of WT and *fer-4* root epidermal cells before and during salt treatment. A local polynomial regression fitting with the 95% confidence interval (gray) was used to represent the distribution curve. n ≥ 5. KPas, 1000 Pascal units.

See also Figure S4.

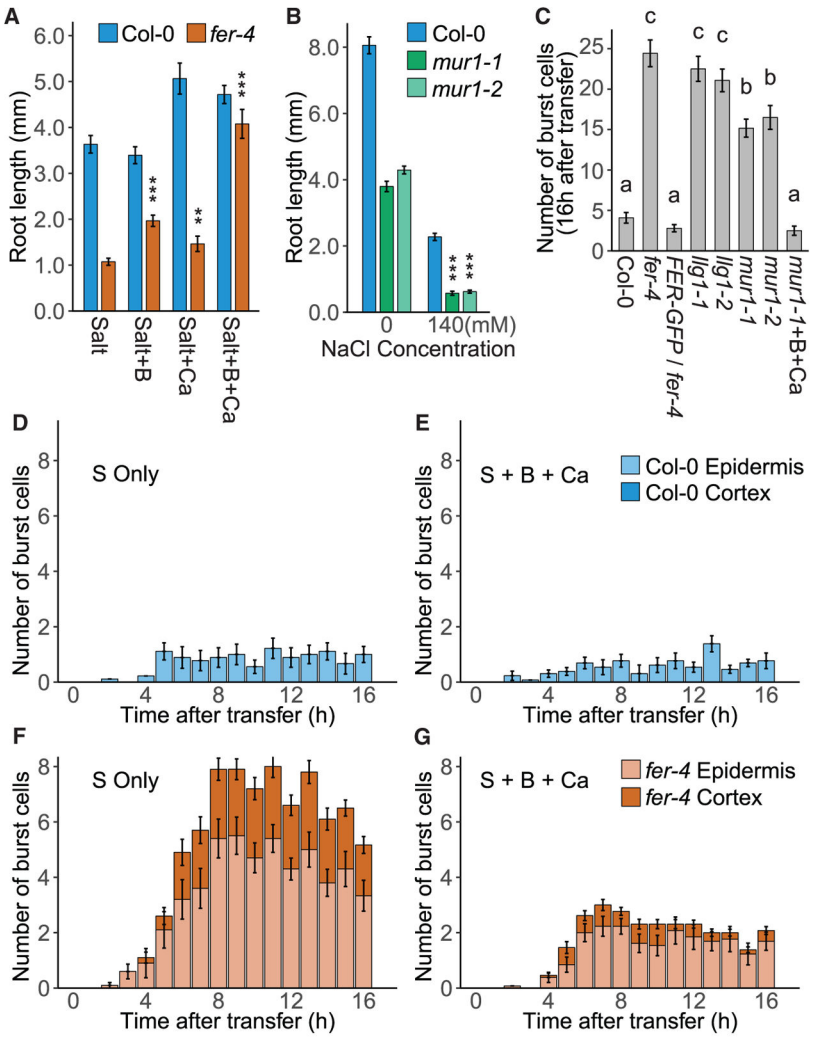

Figure 4. Borate Treatment Prevents Cell Bursting in *fer* and *mur1* Mutants during Salt Stress

(A) Root growth of WT and *fer-4* mutant 2 days after transfer to NaCl media with or without supplementary $CaCl_2$ or boric acid. Salt (S), 140 mM NaCl; Ca, 5 mM $CaCl_2$; B, 3 mM boric acid. n ≥ 15. (**p < 0.01, ***p < 0.001, two-way ANOVA compared to WT and salt-only treatment.)

(B) Root growth of WT and two *mur1* alleles 24 hr after transfer to media with or without 140 mM NaCl. n ≥ 16. (***p < 0.001, two-way ANOVA compared to WT and control treatment.)

(C) Number of burst cells observed within the first 16 hr after salt treatment in WT, *fer-4*, a *FER* complemented line, two *llg1* alleles, two *mur1* alleles, and *mur1-1* supplemented with 5 mM $CaCl_2$ and 3 mM boric acid using wide-field microscopy. Significantly different groups are denoted with different letters ($p < 0.05$). n ≥ 7.

(D–G) Quantification of burst cells from time-lapse imaging of LTI6-YFP-expressing WT (D and E) and *fer-4* (F and G) roots transferred to NaCl mediawith or without supplementary $CaCl_2$ and boric acid. n ≥ 10.

Error bars indicate SEM. See also Figure S4.

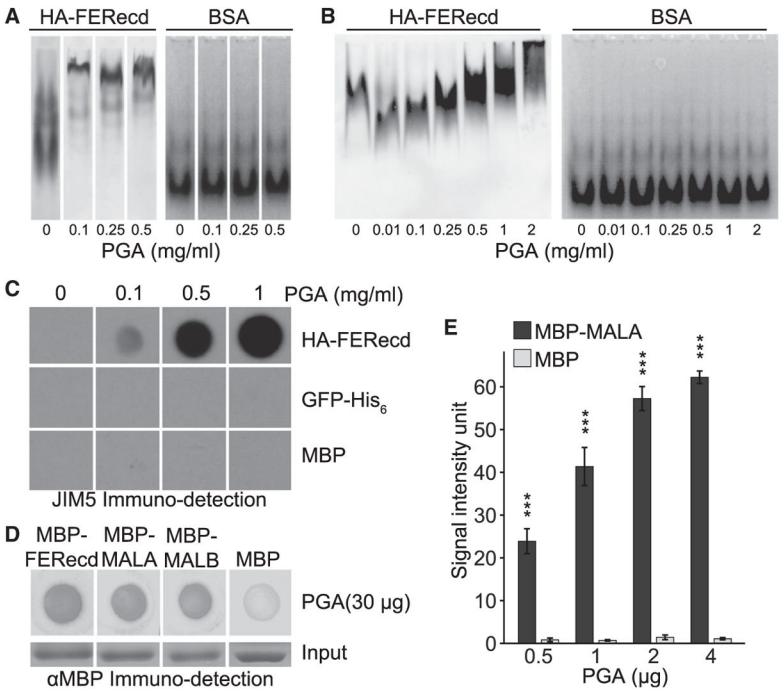

Figure 5. FER Extracellular Domain Interacts with Pectin *In Vitro*

(A) In-gel affinity electrophoresis. Equal amounts of purified HA-FERecd (Figure S5B) or BSA were electrophoresed in native polyacrylamide gels polymerized in the presence of different PGA concentrations.

(B) Electrophoretic mobility shift assay. Purified HA-FERecd or BSA was mixed with different concentrations of PGA prior to electrophoresis on a native polyacrylamide gel.

(C and D) Representative images of dot-blot assays.

(C) HA-FERecd or control proteins (GFP-His_6 and MBP) were immobilized on polyvinylidene fluoride (PVDF) filters and incubated with increasing concentrations of PGA. Pectin bound to the protein dots was detected by JIM5 antibody.

(D) PGA were immobilized on nitrocellulose filters, which were then incubated with FER-derived protein domains or control (MBP). Proteins bound to pectin dots were detected by anti-MBP antibody.

(E) Quantification of a typical dot-blot assay (Figure S5D) showing dose-dependent binding of the FERecd to heat-fragmented PGA. Error bars indicate SEM. (***$p < 0.001$, Student's t test compared to MBP control.)

See also Figure S5.

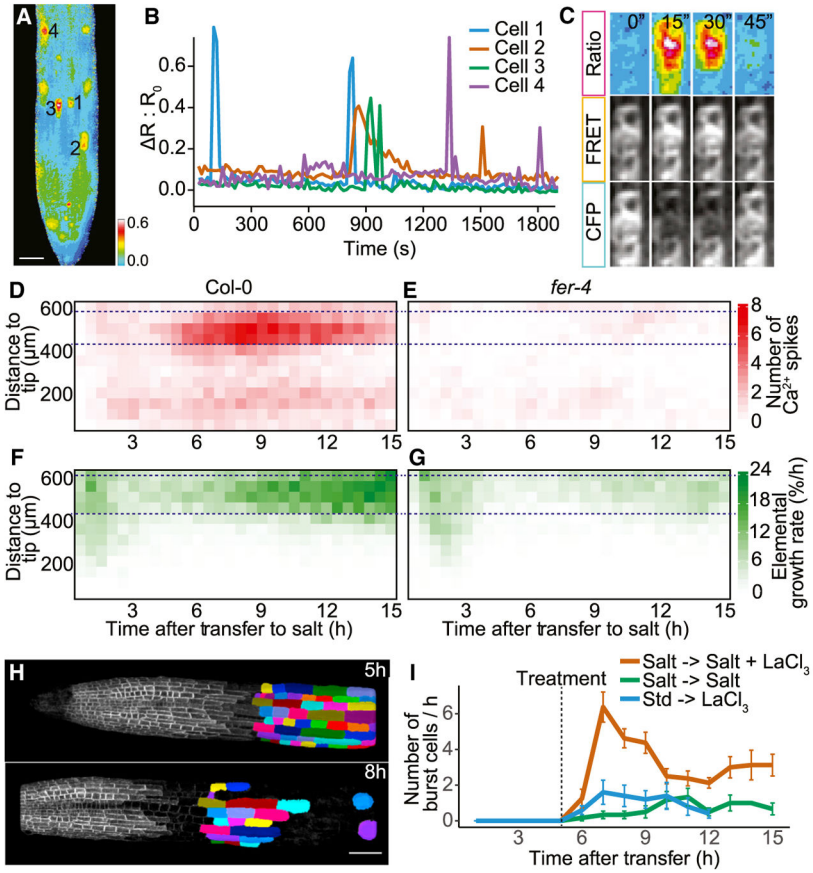

Figure 6. *FER*-Dependent Cell-Specific Calcium Transients Occur during Growth Recovery and Are Necessary to Maintain Cell-Wall Integrity

(A) Maximum-intensity projections of 120 FRET: CFP ratio images (30 min) of a YC3.6-expressing WT root after transfer to media containing 140 mM NaCl. Scale bar, 50 μm.

(B) Δ R:R_0 ratio change of the 4 cells labeled in (A) over the course of 30 min during salt treatment.

(C) Time-lapse images of cell 3 in (A) showing the FRET:CFP ratio, FRET, and CFP images.

(D and E) Heatmaps showing the average number of [Ca^{2+}] spikes in cells of WT (D) and *fer-4* (E) roots in each 50-μm longitudinal zone during each 30-min time window after transfer to media containing 140 mM NaCl. n = 10. Purple lines mark the early elongation zone used for analysis in Figure S6D.

(F and G) Heatmaps showing the average elemental growth rate of WT (F) and *fer-4* (G) roots in each 50-μm longitudinal zone during each 30-min time window after transfer to media containing 140 mM NaCl. n = 10. Purple lines mark the early elongation zone used for analysis in Figure S6E.

(H) Time-lapse images of LTI6-YFP-expressing WT roots pre-treated with 140 mM NaCl for 5 hr, and then transferred to media containing 140 mM NaCl and 0.5 mM $LaCl_3$. Individual epidermal cells at each time point are identified by the same color after image segmentation in MorphoGraphX. Scale bar, 50 μm.

(I) Quantification of burst cells from time-lapse imaging with LTI6-YFP-expressing WT roots during different treatments. Imaging starts 5 hr after the first treatment. Salt, 140 mM NaCl; $LaCl_3$, 0.5 mM $LaCl_3$; Std, standard. $n \geq 6$. Error bars indicate SEM.
See also Figures S6 and S7 and Movies S2, S3, and S4.

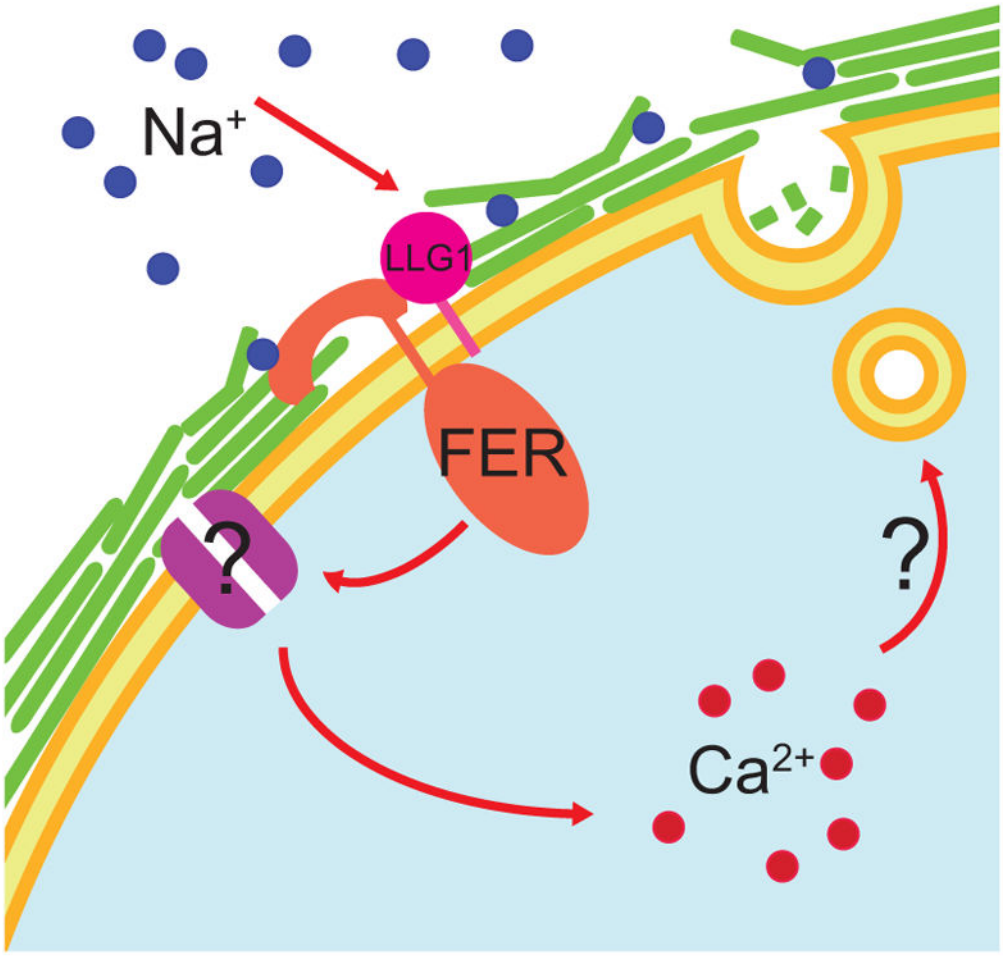

Figure 7. A Model for How FER Signaling Regulates Cell-Wall Integrity under High Salinity

Sodium ions disrupt wall structure, which is sensed by the extracellular domain of FER together with its co-receptor, LLG1. This triggers the activation of an unknown calcium channel resulting in cell-specific [Ca^{2+}] transients during the growth recovery phase. A cell-wall repair mechanism is activated to reinforce wall strength, allowing cells to maintain integrity during cell expansion. See also Table S1 and Data S1.